Progress In Electromagnetics Research C, Vol. 110, 103–117, 2021

Triple Band Dual Sense Circularly Polarized Ceramic Based Antenna: Exploring Conceptual Design Methodology

Anand Sharma[1, *], Gourab Das[2], and Ravi K. Gangwar[2]

Abstract—In this communication, conceptual design guidelines for a tri-band dual sense circularly polarized ceramic-based antenna is explored. An asymmetrical S-shaped aperture is used to stimulate the ring-shaped ceramic. Some exclusive features are obtained in the designed antenna: (i) creation of five different hybrid modes ($HEM_{11\delta}$, $HEM_{11\delta+2}$, $HEM_{12\delta\text{-like}}$, $HEM_{12\delta}$, and $HEM_{13\delta}$) is helpful for getting dual wideband impedance bandwidth; (ii) proposed aperture assists in achieving CP waves in three different frequency ranges with two different senses. Its experimental results confirm the simulated outcomes. The proposed antenna is operated within the dual-frequency ranges, i.e., 2.2–4.19 GHz and 4.74–6.11 GHz, respectively. The measured 3-dB axial ratio is achieved in three different frequency ranges within the operating band, i.e., 2.71–2.98 GHz, 3.6–3.79 GHz, and 5.5–5.81 GHz, respectively. The proposed antenna design is left-handed circularly polarized (LHCP) in the first and third frequency ranges, while it is right-handed in the second one. These features, along with broadsided far-field patterns, recommend the proposed antenna design for potential application in WLAN (2.4/5.5 GHz) and WiMAX (3.3/5.0 GHz) wireless networks.

1. INTRODUCTION

In the current wireless world, dielectric resonator antenna (DRA) has high potential due to its natural proficiencies such as high efficiency, ease of integration with various excitation mechanisms, and supporting a wide variety of mode patterns [1, 2]. Modern wireless communications are also towards the clubbing of circular polarization (CP) features with printed antennas. It is because of its ability to diminish multipath fading with the help of making transmitter and receiver orientation independent [3]. Therefore, the research on DRA in collaboration with CP waves has been a topic of wide interest.

In the case of CP DRAs, the research is widely concentrated on getting wideband/multiband CP characteristics. Recently, designing multiband CP DRAs has been receiving much interest because of its ability to achieve multiple frequency bands with a high signal to noise ratio. Two different methods have been used to obtain multiple frequency bands in the case of ceramic-based antennas, i.e., hybrid radiator [4, 5] and multi-mode radiator [6]. Zuo et al. proposed a hybrid DRA, which was the grouping of cross-aperture and rectangular-shaped ceramic. Cross-aperture has been worked as both radiators and excitation structure. The presented radiator worked in dual-frequency bands, i.e., 1.9 GHz and 2.7 GHz, respectively [4]. Pan et al. designed a hybrid DRA, which is the combination of a metallic patch and ceramic material. It operated in two different frequency bands, i.e., 1.87–1.92 GHz and 2.22–2.66 GHz [5]. Fang et al. presented an aperture coupled grooved rectangle-shaped ceramic material with dual-band circular polarization features. In above-mentioned antenna structure, dual-band characteristics were obtained through dual-mode generation, i.e., quasi-TE_{111} and TE_{113} [6]. Most of the DRA-based CP

Received 5 December 2020, Accepted 9 February 2021, Scheduled 22 February 2021
* Corresponding author: Anand Sharma (anandsharma@mnnit.ac.in).
[1] Department of Electronics and Communication Engineering, Motilal Nehru National Institute of Technology Allahabad, Prayagraj, Uttar Pradesh 211004, India. [2] Department of Electronics Engineering, Indian Institute of Technology (Indian School of Mines) Dhanbad, Jharkhand 826004, India.

antennas available in the open literature generate dual-band CP wave. Very few articles are available where triple or more CP characteristics are excited in a single antenna structure [7–10]. Altaf et al. presented a triple-band CP antenna with reconfigurability. The use of pin diodes made the design more complex [7]. Cheng et al. proposed a tri-band omnidirectional CP DRA with top-loaded loops [8]. The top-loaded loops acted as a horizontally placed magnetic dipole and helped to achieve triple-band CP. Sharma et al. proposed a dual-band dual sense ceramic based radiator. In order to achieve it, a Swastika-shaped aperture is used as the feeding structure, which stimulates $HEM^{x}_{11\delta}$ and $HEM^{y}_{11\delta}$ inside the ceramic material [9]. Sharma et al. proposed aperture coupled cylindrical DRA to achieve quad-band CP waves. It was based on the multi-mode generation technique. However, this antenna suffered from large physical size, i.e., $120 \times 120\,\text{mm}^2$ [10].

In this article, a step by step analysis of an aperture coupled ring shaped ceramic antenna is explained. This antenna is designed to produce triple-band CP waves along with dual sense appearances. Stimulation of the ring-shaped ceramic with asymmetric S-shaped aperture provides two unique features: (i) formation of five various hybrid mode patterns, i.e., $HEM_{11\delta}$, $HEM_{11\delta+2}$, $HEM_{12\delta\text{-like}}$, $HEM_{12\delta}$, and $HEM_{13\delta}$; and (ii) triple-band dual sense CP waves are also created. The remainder of the paper is organised as follows: (a) geometrical layout of the proposed radiator; (b) design methodology of the proposed radiator; (c) its detailed analysis; (d) its experimental outcomes and comparison with simulated results; and (e) conclusion.

2. GEOMETRICAL LAYOUT OF THE PROPOSED TRIPLE BAND CP ANTENNA

The geometrical layout of the proposed triple-band dual sense ceramic-based CP antenna is presented in Fig. 1. An asymmetrical S-shaped aperture and simple microstrip line have been etched on the upper and lower parts of an FR-4 substrate, respectively. The permittivity and loss tangent ($\tan\delta$) of the FR-4

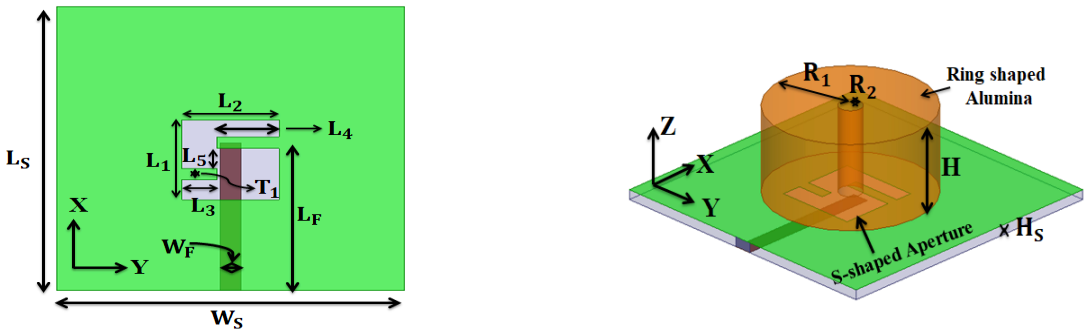

Figure 1. Geometrical layout of proposed triple band CP antenna. (a) Asymmetrical S-shaped aperture, (b) 3D view.

Figure 2. Pictures of fabricated triple band CP antenna. (a) Bottom view, (b) top view.

substrate are 4.4 and 0.02, respectively. Ring-shaped alumina material ($\varepsilon_{Alumina} = 9.8$; $\tan\delta = 0.002$) has been jammed over the substrate with the help of paste, i.e., Fevi-Quick. The inner ($R2$) and outer ($R1$) radii of ring-shaped ceramic are 2.0 mm and 14.0 mm, respectively, whereas the height, denoted by H, is 14.0 mm. Its prototype has also been designed for experimental verification, and its pictures are shown in Fig. 2. Dimensions of some of the important parameters of proposed ceramic-based antenna are: $L_S = W_S = 50$ mm; $L_1 = L_2 = 15.0$ mm; $H_S = 1.6$ mm; $L_3 = 5.0$ mm; $L_4 = 8.0$ mm; $L_5 = 3.5$ mm; $T_1 = 2.0$ mm; $L_F = 26.0$ mm; $W_F = 3.0$ mm.

3. DESIGN METHODOLOGY

The design methodology of the proposed radiator is classified into two stages: (i) Multiple Hybrid mode generation; and (ii) CP wave generation.

3.1. Multiple Hybrid Mode Generation

Following three-step procedure is utilized in order to generate multiple hybrid modes in the proposed antenna design:

Step-1: Narrow rectangular aperture coupled ring-shaped ceramic material acts as a magnetic dipole and creates $\text{HEM}_{11\delta}$ mode in ring DRA. Due to the large current density near the edges of the aperture, it creates one more mode, i.e., $\text{HEM}_{12\delta\text{-like}}$ mode.

Step-2: In this step, narrow rectangular aperture is converted into a square-shaped aperture. This aperture performs as both electric and magnetic dipoles. Such type of feed mechanism is helpful for generating the entire aforementioned mode, i.e., $\text{HEM}_{11\delta}$, $\text{HEM}_{12\delta\text{-like}}$, and $\text{HEM}_{12\delta}$ modes. Due to the broadening of aperture dimension, satisfying the boundary condition for vanishing E-field due to the metallic ground plane as well as the large height of ring ceramic allows the higher-order mode, i.e., $\text{HEM}_{11\delta+2}$ and $\text{HEM}_{13\delta}$.

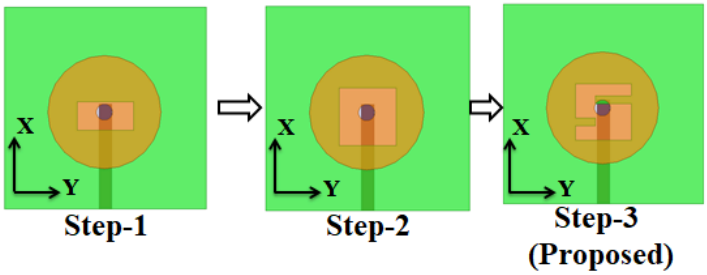

Figure 3. Designing steps for proposed triple band CP antenna.

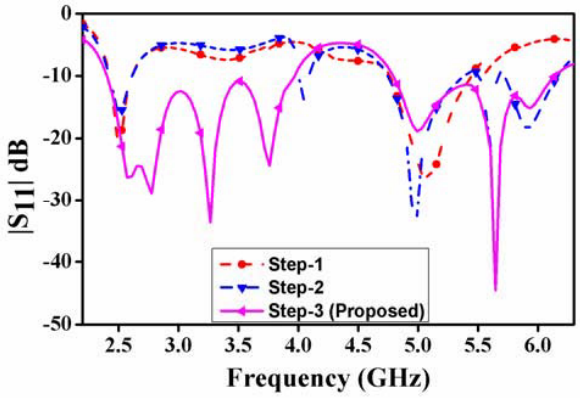

Figure 4. $|S_{11}|$ variation for different design steps.

Step-3: Two metallic strips of unequal lengths are added with a square-shaped aperture (asymmetrical S-shaped aperture). This creates orthogonal degenerated modes with a 90° phase shift. Due to the introduction of path delay with unequal metallic strip, two more resonant peaks are observed in the spectrum, i.e., $HEM^{y}_{11\delta}$ and $HEM^{y}_{11\delta+2}$. Practically, two modes are said to degenerate, if the ratio of resonant frequencies lies in between 1.01 and 1.10 [11]. All these four steps are displayed in Fig. 3, and resultant $|S_{11}|$ variation is shown in Fig. 4.

3.2. CP Wave Generation

To generate CP waves in any radiating structure, two conditions are to be satisfied: (i) generation of degenerated orthogonal modes with equal amplitude; and (ii) 90° phase shift between them [3]. Adding two metallic strips on the opposite faces of square aperture creates orthogonal modes inside the ceramic material. Unequal length of metallic strip helps to get 90° phase shift between the orthogonal modes. Fig. 5 shows three different steps for obtaining the CP waves. In step-1, a square-shaped aperture is used to excite the ceramic material. On the other hand, step-2 and step-3 consist of square apertures with one strip and two strips, respectively.

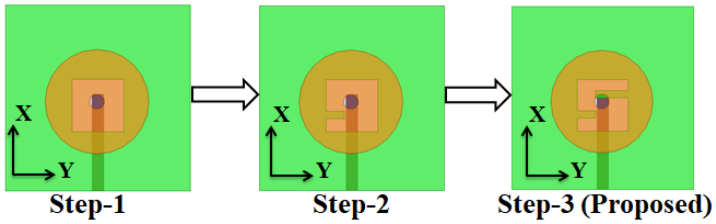

Figure 5. Different steps involved for getting CP wave in proposed antenna.

Figure 6 shows the axial ratio variation over the working frequency band. As clear in the figure, it is confirmed that CP waves are generated in three different frequency bands due to the square-shaped aperture with two strips. The complete design methodology is displayed in Fig. 7. Two important observations are obtained from Fig. 7: (i) wide square aperture is able to stimulate five different hybrid radiating modes in ring-shaped ceramic; and (ii) transition from square aperture to asymmetrical S-shaped aperture converts the proposed antenna from linear to circular polarization.

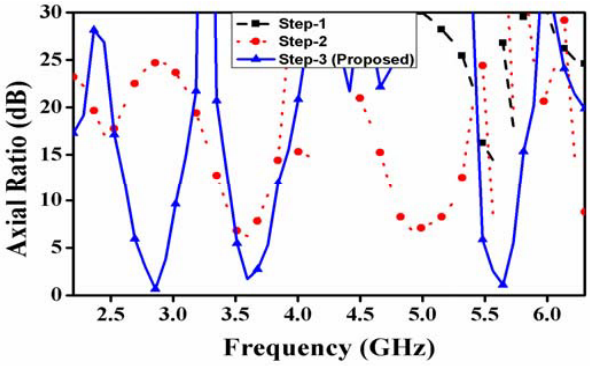

Figure 6. Axial ratio variations for different steps involved for getting CP wave in proposed antenna ($\theta = 0°$; $\varphi = 0°$).

4. DETAILED ANALYSIS OF THE PROPOSED ANTENNA

In this section, detailed mathematical, as well as theoretical analysis of proposed antenna, has been carried out using Ansys HFSS EM simulator. Before starting any analysis, it is important here to confirm

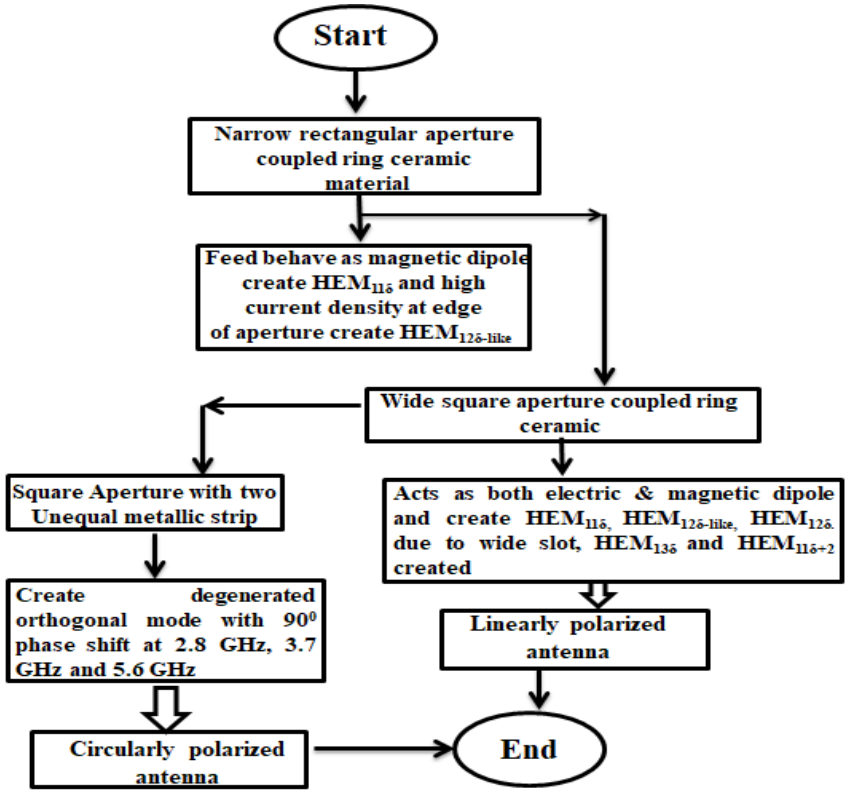

Figure 7. Flowchart for design methodology of proposed antenna.

the accountability of different resonances because aperture can also act as resonating structure. For this purpose, Fig. 8 presents $|S_{11}|$ variations of proposed antenna with and without Alumina ceramic. From Fig. 8, it is confirmed that alumina-based ceramic material is accountable for all the resonances present in the spectrum. Another important observation obtained from Fig. 8 is that ring-shaped ceramic material delivers improved impedance bandwidth as compared to cylindrical shaped ceramic in the operating frequency bands. This modification in ceramic shape also slightly adjusts the resonant frequency due to the change in effective permittivity. It can be understood, mathematically, as follows [12]:

$$\varepsilon_{\text{ring DRA}} = \left[\frac{\varepsilon_{\text{Alumina}}(V_{\text{Alumina}}) + V_{\text{air-cavity}}}{V_{\text{Alumina}} + V_{\text{air-cavity}}}\right] \tag{1}$$

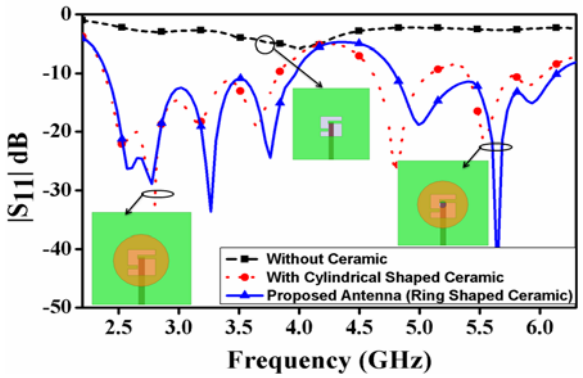

Figure 8. $|S_{11}|$ variations of the proposed antenna with and without Alumina ceramic.

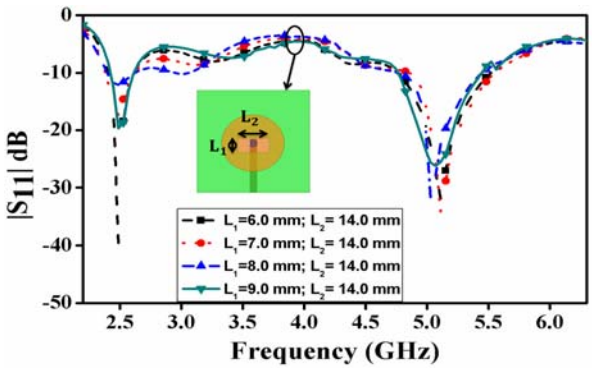

Figure 9. $|S_{11}|$ variation of narrow rectangular aperture coupled ring-shaped ceramic material with change in L_1.

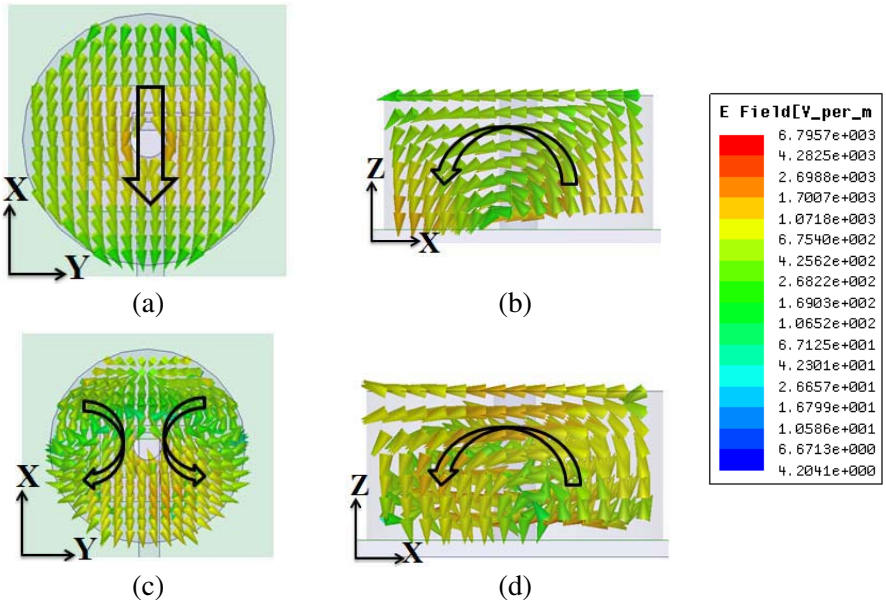

Figure 10. Near field distribution on ring shaped ceramic. (a) Upper view at 2.55 GHz, (b) adjacent view at 2.55 GHz, (c) upper view at 5.0 GHz, (d) adjacent view at 5.0 GHz.

$$V_{\text{Alumina}} = V_{\text{Cylindar}} - V_{\text{air-cavity}} \tag{2}$$

In Eqs. (1) and (2), 'V_{Alumina}' and '$V_{\text{air-cavity}}$' are the volumes of cylinder-shaped solid sections of alumina and air-cavity, respectively. From the above-mentioned equations, it is mathematically confirmed that '$\varepsilon_{\text{ring DRA}}$' is lower than '$\varepsilon_{\text{Alumina}}$'. It is known that impedance bandwidth is inversely proportional to the effective permittivity [3].

Figure 9 shows $|S_{11}|$ variation of narrow rectangular aperture coupled ring-shaped ceramic material change in length (L_1). From Fig. 9, it is confirmed that in the aforementioned case, dual resonating peaks are created at 2.55 GHz and 5.0 GHz, respectively.

Figure 10 displays the near-field distribution on ring-shaped ceramic at 2.55 GHz and 5.0 GHz. From Fig. 10, it is confirmed that $\text{HEM}_{11\delta}$ and $\text{HEM}_{12\delta\text{-like}}$ modes are accountable for resonant peaks at 2.55 GHz and 5.0 GHz, respectively [13, 14]. In order to understand the physics behind the creation of $\text{HEM}_{11\delta}$ mode, let us see the E- and H-field spreading on the narrow rectangular aperture at 2.55 GHz in Fig. 11. From E- and H-field distributions, it is clear that TE_{10} mode is generated in this case. For this mode, tangential electric field distribution (E_S), as well as surface electric (JS) and magnetic (MS) current density across the aperture, is given as follows [3]:

$$E_S = E_0 \cos\left(\frac{\pi}{L_2 y}\right) \left\{ \begin{array}{l} -L_1/2 \le X \le L_1/2 \\ -L_2/2 \le Y \le L_2/2 \end{array} \right\} \tag{3}$$

$$M_S = \left\{ \begin{array}{ll} -2\hat{n} \times E_S & \left\{ \begin{array}{l} -L_1/2 \le X \le L_1/2 \\ -L_2/2 \le Y \le L_2/2 \end{array} \right\} \\ 0 & \text{elsewhere} \end{array} \right\} \tag{4}$$

$$J_S = 0 \quad \text{everywhere} \tag{5}$$

From Eqs. (3)–(5), it is confirmed that the narrow rectangular aperture behaves as a magnetic dipole. It is a well known fact that if the feed behaves as a magnetic dipole, then it generates $\text{HEM}_{11\delta}$ mode inside the ring-shaped ceramic [15]. The E-field line at 5.0 GHz is approx. same as $\text{HEM}_{12\delta}$. However, due to high field distribution at the edges of the aperture, E-field lines rotate towards the ground, which is not the case of $\text{HEM}_{12\delta}$ mode. Therefore, this mode is generally called as $\text{HEM}_{12\delta\text{-like}}$ mode [14].

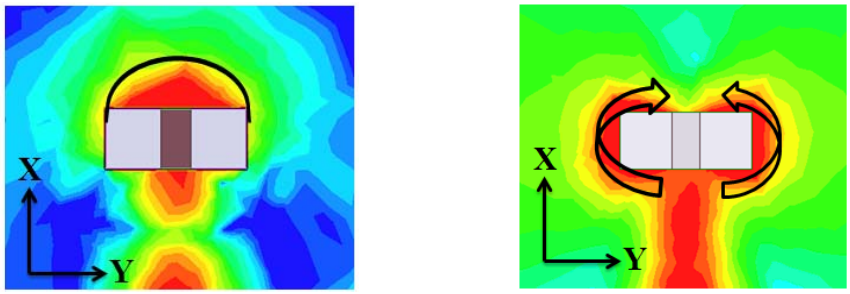

(a) (b)

Figure 11. Field distribution over the aperture at 2.55 GHz. (a) E-field, (b) H-field.

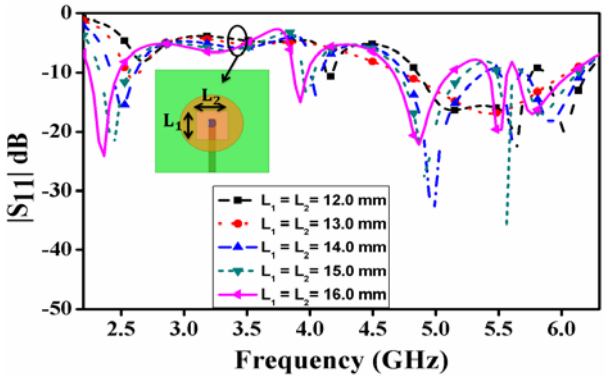

Figure 12. $|S_{11}|$ variation of square aperture coupled ring-shaped ceramic material with change in length ($L_1 = L_2$).

Mathematically, the resonant frequency of $\text{HEM}_{11\delta}$ mode is calculated as follows [15]:

$$f_{r,\text{HEM}_{11\delta}} = \frac{6.324c}{4\pi R_1\sqrt{\varepsilon_{\text{ring DRA}}+2}}\left\{0.27+0.36\left(\frac{R_1}{2H}\right)+0.02\left(\frac{R_1}{2H}\right)^2\right\} \tag{6}$$

From Eq. (6), it is found that mathematically, $\text{HEM}_{11\delta}$ mode is obtained at 2.76 GHz for the same ring-shaped ceramic material. It is closer to the simulated obtained value. Resonant frequency of $\text{HEM}_{12\delta\text{-like}}$ mode cannot be calculated mathematically because of the non-availability of the empirical formula.

Figure 12 shows the reflection coefficient ($|S_{11}|$) variation for wide square-shaped slot excited ring ceramic. From Fig. 12, it is observed that apart from the resonant peak created due to narrow rectangular aperture, three different resonant peaks are created at 3.9 GHz, 5.6 GHz, and 5.8 GHz, respectively.

In order to find out the accountability of resonant peak at 5.6 GHz, Fig. 13 shows the near-field distribution on the ring-shaped ceramic. It is clearly observed from Fig. 13 that the $\text{HEM}_{12\delta}$ mode is exited at 5.6 GHz [12]. To understand the generation mechanism of the $\text{HEM}_{12\delta}$ mode, Fig. 14 displays the E-field and H-field distributions over the square aperture at 5.6 GHz. From Fig. 14, it can be observed that the E-field distribution of wide square aperture is same as H-field of narrow rectangular aperture at 5.6 GHz. According to Babinet's principle, interchanging of E- and H-fields confirms the electric dipole nature of wide square aperture [3]. There is no empirical formula available for $\text{HEM}_{12\delta}$ mode. However, it can be expected with the assistance of the resonant frequency of $\text{HEM}_{11\delta}$ mode and aspect ratio of ring shaped ceramic. In the proposed antenna, aspect ratio of ring shaped ceramic is 1.0. For such ceramic, the resonant frequency of $\text{HEM}_{12\delta}$ mode can be predicted as follows [10]:

$$f_{r,\text{HEM}_{12\delta}} = 1.9 \times f_{r,\text{HEM}_{11\delta}} \tag{7}$$

From Eq. (7), the frequency of $\text{HEM}_{12\delta}$ mode is found to be 5.33 GHz, which is fairly close to simulated results.

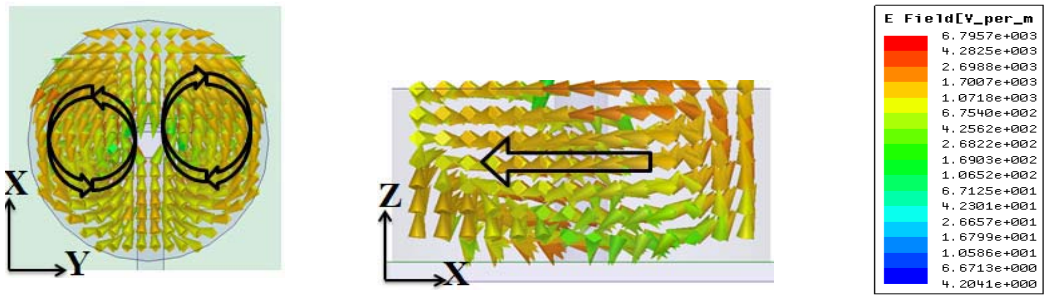

(a) (b)

Figure 13. Near field distribution on ring-shaped ceramic. (a) Top view at 5.6 GHz, (b) side view at 5.6 GHz.

(a) (b)

Figure 14. Field distribution over the aperture at 5.6 GHz. (a) E-field, (b) H-field.

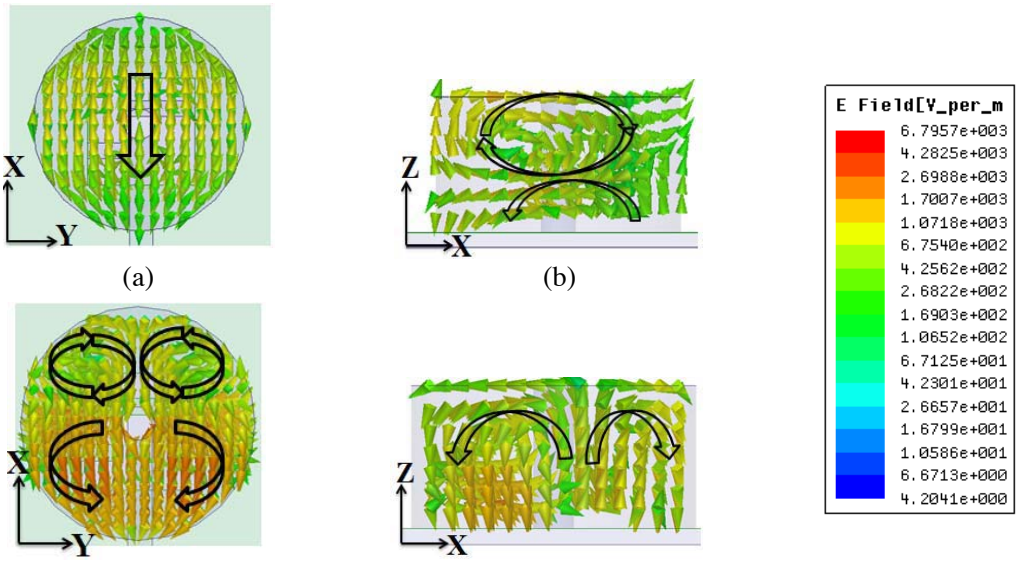

(a) (b)

(c) (d)

Figure 15. Near field distribution on ring-shaped ceramic. (a) Top view at 3.9 GHz, (b) side view at 3.9 GHz, (c) top view at 5.8 GHz, (d) side view at 5.8 GHz.

Figure 15 displays the near-field distribution at 3.9 GHz and 5.8 GHz, respectively. Fig. 15 confirms that $HEM_{11\delta+2}$ and $HEM_{13\delta}$ modes are obtained at 3.9 GHz and 5.8 GHz. It is well known that $HEM_{11\delta+2}$ and $HEM_{13\delta}$ are the higher-order modes of $HEM_{11\delta}$ [10, 16]. Therefore, it is formed because of the magnetic dipole nature of the feeding mechanism. It should be highlighted that a wider aperture allows to produce higher order modes. However, in the proposed antenna design, the size of the square

aperture is much smaller than ground plane. Accordingly, the boundary conditions satisfy the required boundary condition for both the $\mathrm{HEM}_{11\delta+2}$ and $\mathrm{HEM}_{13\delta}$ modes due to heavily attenuated tangential E-field on the ground plane [16].

There is no mathematical formula available for calculating the resonant frequency of $\mathrm{HEM}_{11\delta+2}$ and $\mathrm{HEM}_{13\delta}$ modes. However, they are the higher-order modes of $\mathrm{HEM}_{11\delta}$. Therefore, their resonant frequencies can be predicted as follows [17]:

$$f_{r,\mathrm{HEM}_{11\delta+2}} = 1.5 \times f_{r,\mathrm{HEM}_{11\delta}} \tag{8}$$

$$f_{r,\mathrm{HEM}_{13\delta}} = 1.5 \times f_{r,\mathrm{HEM}_{11\delta+1}} + (f_{r,\mathrm{HEM}_{11\delta+1}} - f_{r,\mathrm{HEM}_{11\delta}}) \tag{9}$$

$\mathrm{HEM}_{11\delta+2}$ mode is the second higher-order mode of $\mathrm{HEM}_{11\delta}$, so its resonant frequency is 1.5 times of fundamental mode. From Eqs. (8) and (9), the resonant frequencies of $\mathrm{HEM}_{11\delta+2}$ and $\mathrm{HEM}_{13\delta}$ modes are found to be 4.1 GHz and 5.865 GHz, respectively, which are quite close to simulated value.

Figure 16 shows the $|S_{11}|$ variation of the proposed antenna with the change in length L_4. In the same case, L_3 is fixed. From Fig. 16, it can be observed that as the length of the upper strip (L_4) increases with respect to L_3, two more resonant peaks are generated at 2.84 GHz and 3.4 GHz, respectively. In order to recognize the responsibility of resonances, Fig. 17 shows the near-field distribution at 2.84 GHz

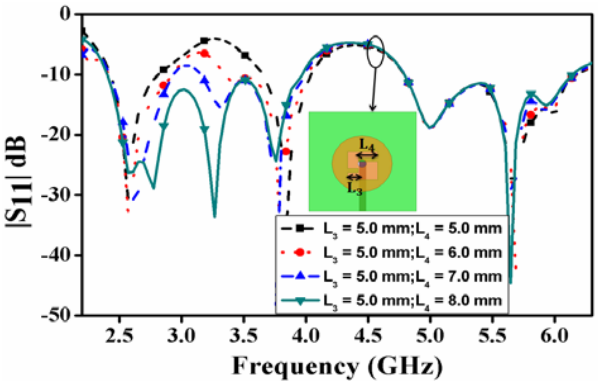

Figure 16. $|S_{11}|$ variation of proposed aperture coupled ring-shaped ceramic with change in length L_4 and fixed L_3.

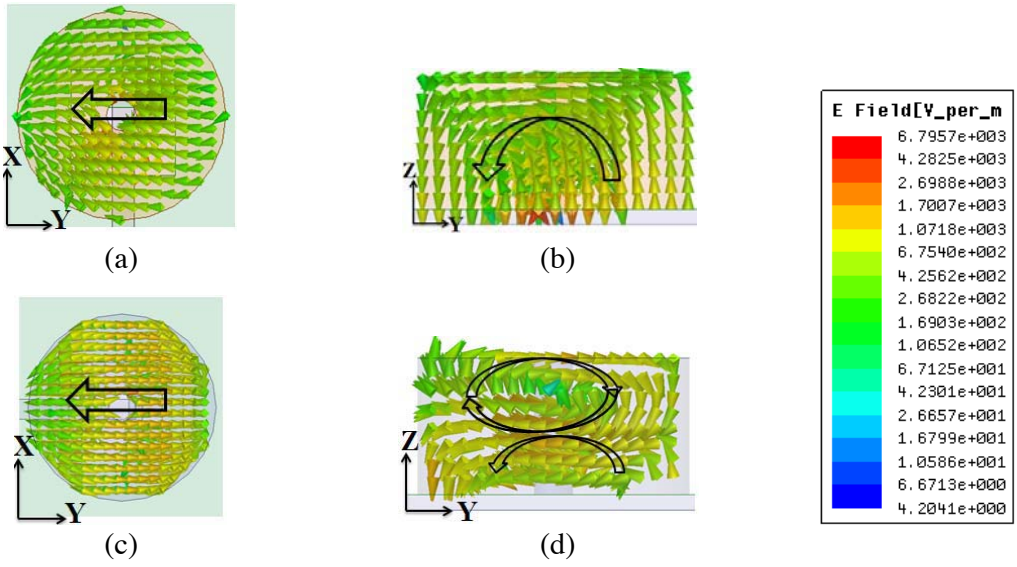

Figure 17. Near field distribution on ring-shaped ceramic. (a) Top view at 2.84 GHz, (b) side view at 2.84 GHz, (c) top view at 3.4 GHz, (d) side view at 3.4 GHz.

and 3.4 GHz, respectively. From Fig. 17, it is confirmed that $HEM^{y}_{11\delta}$ and $HEM^{y}_{11\delta+2}$ are generated at 2.84 GHz and 3.4 GHz, respectively [15, 16]. Upper and lower strips in connection with square-shaped aperture are used to generate orthogonal modes (in order to get CP Waves). That is why these additional resonant peaks are generated.

Figure 18 shows the optimization of CP waves with change in the length of the upper strip, i.e., L_4. Simulation has been done in the broadside direction ($\theta = 0°$; $\varphi = 0°$). As two strips are added with the square-shaped aperture, orthogonal modes are produced (as shown in Fig. 17). From Fig. 18(a), it is seen that as the length (L_4) of the upper strip is more than L_3, 90° phase shift is created between the orthogonal degenerated modes with equal amplitude at three different frequencies, i.e., 2.8 GHz, 3.7 GHz, and 5.6 GHz. It is the necessary condition for CP generation.

Figures 19, 20, and 21 show E-field variations for different phase angles at 2.8 GHz, 3.7 GHz, and 5.6 GHz, respectively. It is clearly observed from Fig. 19 and Fig. 21 that E-field rotates in clockwise direction. On the other hand, it is seen from Fig. 20 that E-field rotates in anticlockwise direction. It simply means that the proposed antenna is left-handed circularly polarized (LHCP) at 2.8 GHz and 5.6 GHz, respectively, while it is right-handed circularly polarized (RHCP) at 3.7 GHz [3].

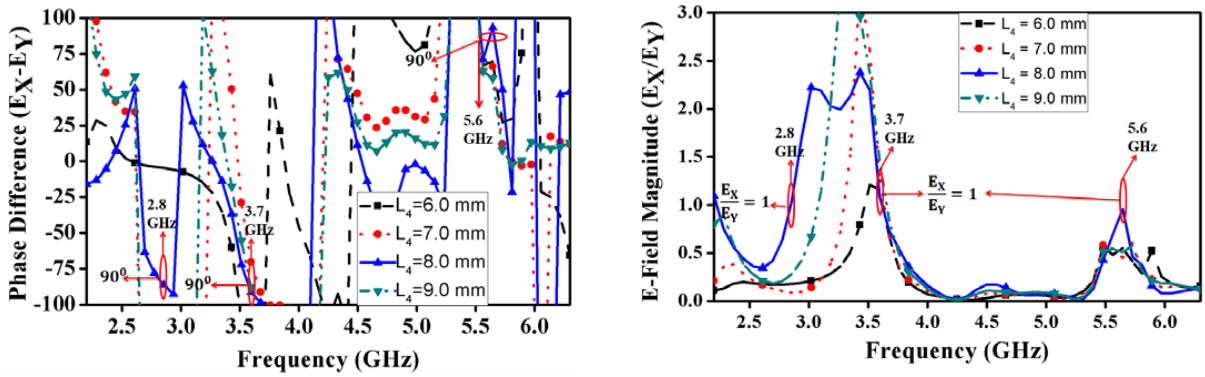

Figure 18. Optimization of CP wave for proposed antenna ($\theta = 0°$; $\varphi = 0°$). (a) Variation in phase difference of E_X and E_Y component, (b) ratio of $|E_X/E_Y|$ for the proposed antenna.

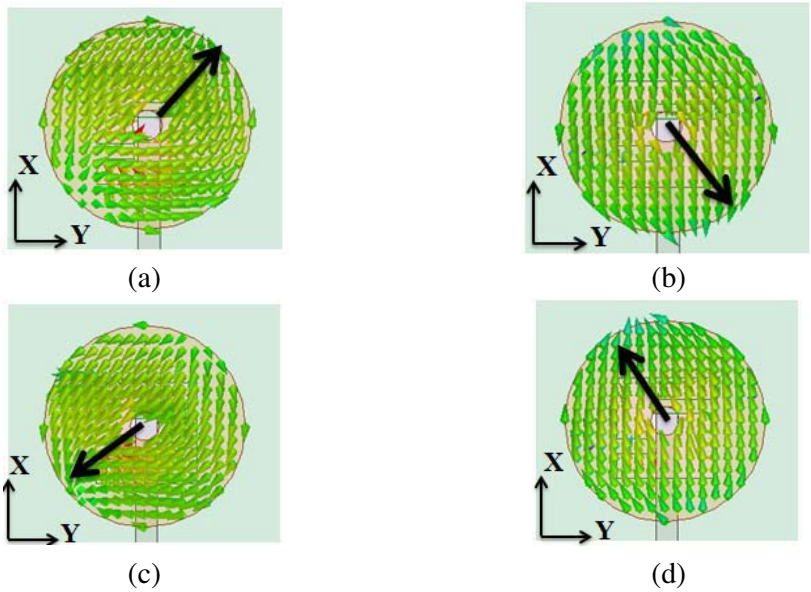

Figure 19. E-field variation at 2.8 GHz. (a) 0°, (b) 90°, (c) 180°, (d) 270°.

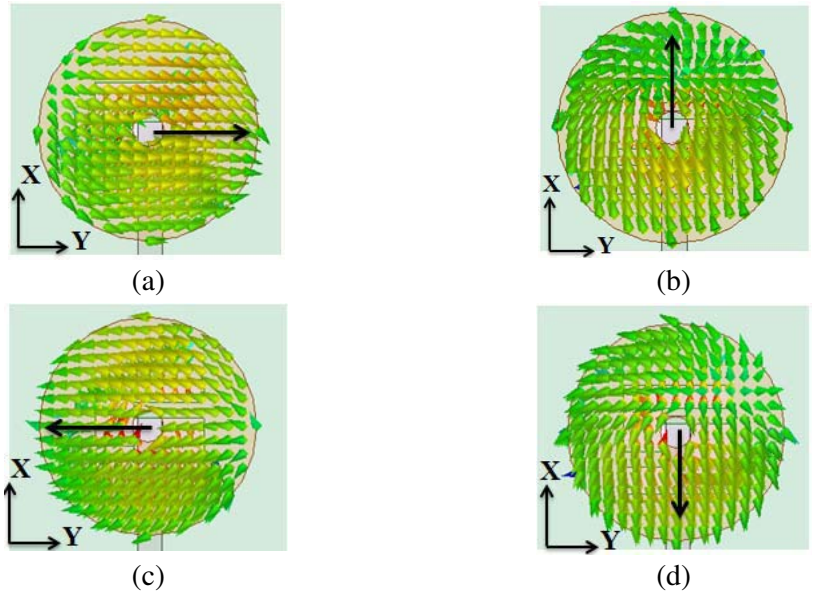

Figure 20. *E*-field variation at 3.7 GHz. (a) 0°, (b) 90°, (c) 180°, (d) 270°.

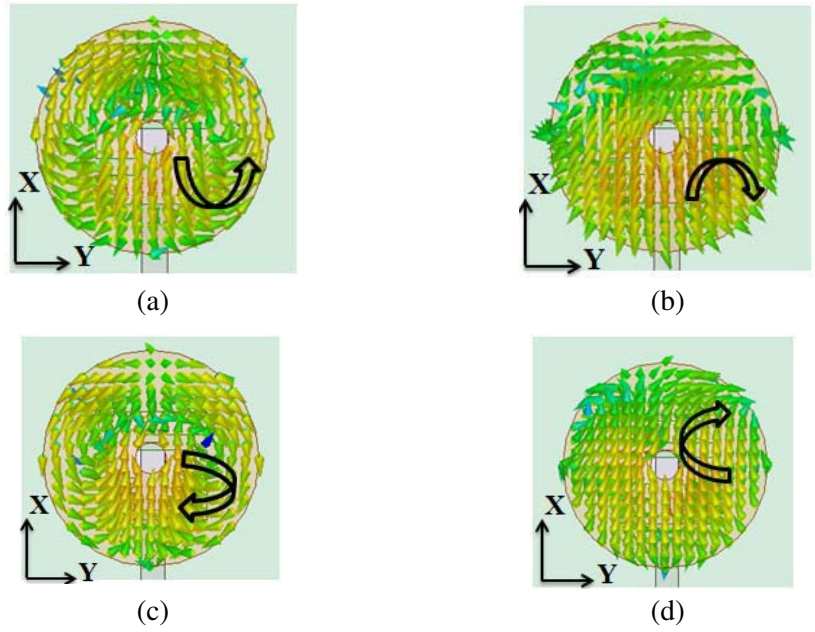

Figure 21. *E*-field variation at 5.6 GHz. (a) 0°, (b) 90°, (c) 180°, (d) 270°.

5. EXPERIMENTAL OUTCOMES

In this section, the experimental outcomes are discussed and compared with numerical simulation outcomes. For this purpose, a prototype of the proposed antenna is fabricated (shown in Fig. 2). Fig. 22 presents the comparison between measured and simulated reflection coefficients curves. Reflection coefficient is measured with the aid of Keysight E5071C VNA. It can be observed from Fig. 22 that the proposed antenna works in two frequency bands, i.e., 2.2–4.19 GHz and 4.74–6.11 GHz, respectively. Some differences have occurred between practically obtained and simulated reflection coefficients. It is due to the use of adhesive for jamming the ceramic material [18].

Figure 23 presents the experimental and simulated axial ratio variations towards the broadside direction ($\theta = 0°$; $\varphi = 0°$). Axial ratio is measured with dual linear pattern measurement method [19]. After seeing Fig. 23, it can be said that the proposed radiator provides CP waves in three different frequency ranges within the working bands, i.e., 2.71–2.98 GHz, 3.6–3.79 GHz, and 5.5–5.81 GHz,

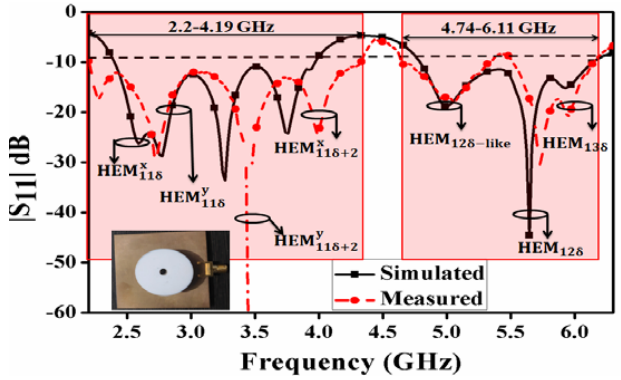

Figure 22. Assessment between experimental and simulated reflection coefficients.

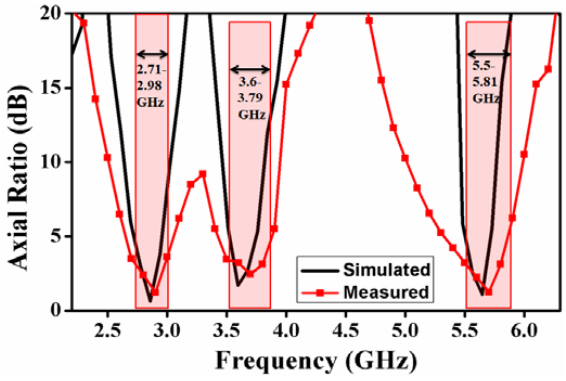

Figure 23. Assessment between experimental and simulated axial ratios towards broadside direction ($\theta = 0°$; $\varphi = 0°$).

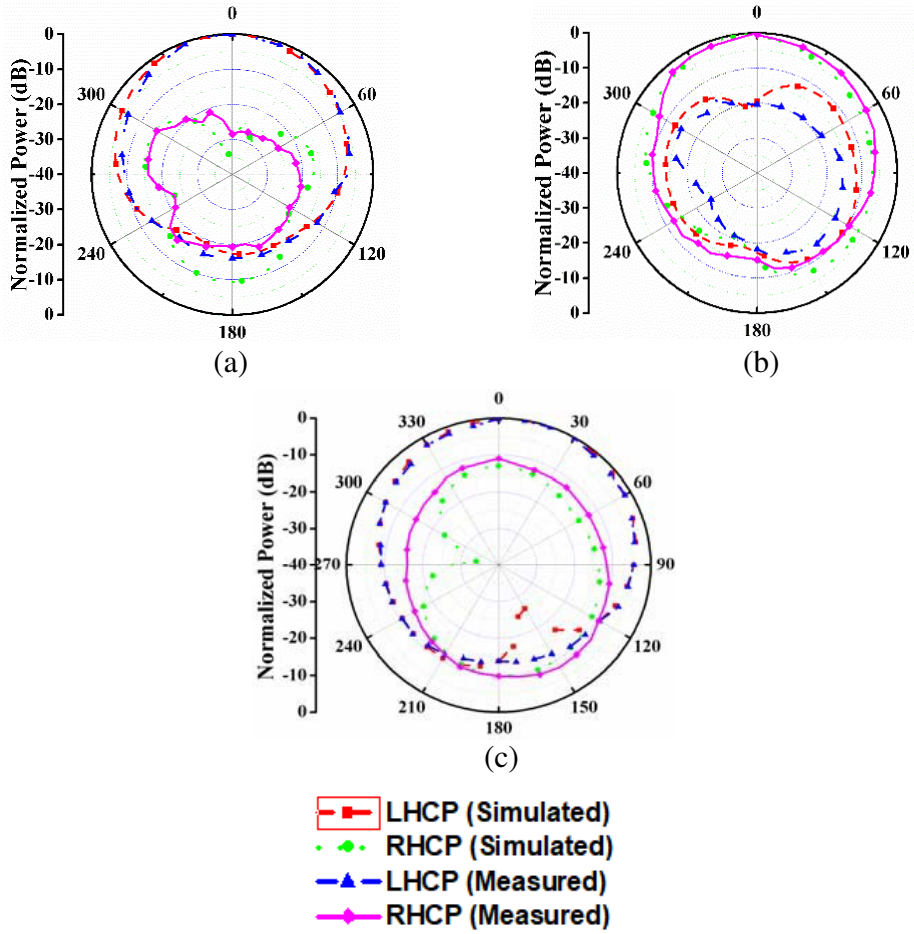

Figure 24. LHCP and RHCP patterns of proposed triple band CP antenna in XZ plane. (a) 2.8 GHz, (b) 3.6 GHz, (c) 5.6 GHz.

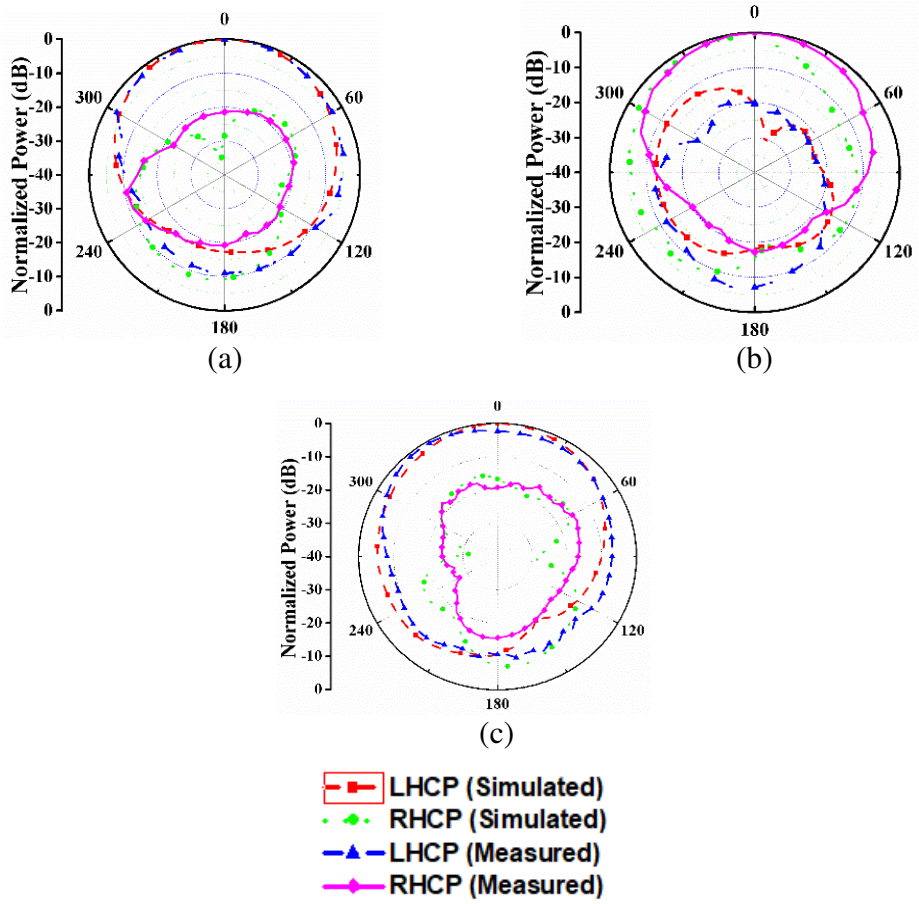

Figure 25. LHCP and RHCP patterns of proposed triple band CP antenna in YZ plane. (a) 2.8 GHz, (b) 3.6 GHz, (c) 5.6 GHz.

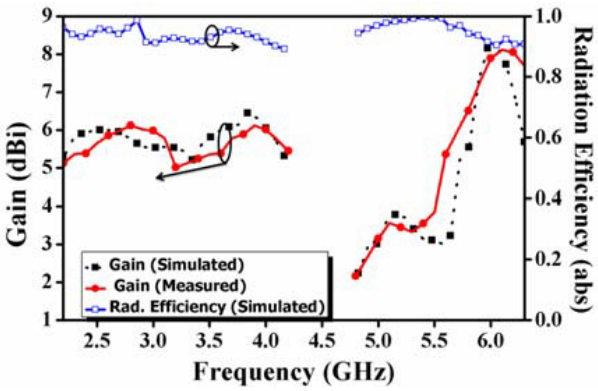

Figure 26. Gain and radiation efficiency graph of proposed triple band CP antenna.

respectively. Slight changes are present between practically obtained and simulated outcomes, which are due to the misalignment between reference and proposed antennas, as well as the use of adhesive.

Figure 24 shows the experimental and simulated LHCP and RHCP patterns at 2.8 GHz, 3.6 GHz, and 5.6 GHz in XZ, respectively. Fig. 2 shows the experimental and simulated LHCP and RHCP patterns at 2.8 GHz, 3.6 GHz, and 5.6 GHz in YZ, respectively. Three remarks are attained from Fig. 24 and Fig. 25: (i) broadsided patterns are obtained at all three frequencies, which confirms the

presence hybrid mode [15]; (ii) LHCP pattern is more dominant (approx. 15 dB) than RHCP at 2.8 GHz and 5.6 GHz; and (iii) RHCP pattern is more dominant (approx. 15 dB) than LHCP at 3.6 GHz. These observations confirm the dual-sensing capability of the proposed radiator.

Figure 26 presents gain (experimental and simulated) and radiation efficiency (simulated) towards the broadside direction. Two-antenna method has been used to measure the gain value [3]. Good agreement is observed between experimental and simulated gain values. The maximum value of gain is about 8.0 dBi for the proposed antenna. Radiation efficiency is greater than 90% in both working bands. Table 1 compares the performance of the proposed antenna with other published ceramic-based CP antennas based on electrical antenna size, impedance, axial ratio bandwidth, and gain. After observing Table 1, it can be said that the proposed radiator has better inclusive performance than other published CP DRAs.

Table 1. Comparison of proposed triple band CP antenna with other existing one.

Shape of Ceramic Material	Excitation Technique	Impedance Bandwidth (%)	AR Band (%)	Antenna Size (mm^2)	Max Gain (dBi)
Rectangular [4]	Aperture	14/12.8	3.0/3.5	$0.44\lambda_0 \times 0.44\lambda_0$	5.5
Cylindrical [5]	Probe	2.64/18.03	3.16/5.06	$0.36\lambda_0 \times 0.36\lambda_0$	1.4
Grooved Rectangular [6]	Aperture	25.3/35.3	6.3/3.68	$0.8\lambda_0 \times 0.8\lambda_0$	8.0
Spandrel Fractal [7]	Probe	14.44/40.48	6.35/6.65/7.09	$1.18\lambda_0 \times 1.77\lambda_0$	5.55
Cylindrical [8]	Probe	1.8/7.8/3.9	1.5/4.9/0.8	$0.58\lambda_0 \times 0.58\lambda_0$	1.6
Cylindrical [9]	Aperture	10.75/16.79	5.45/10.12	$0.29\lambda_0 \times 0.29\lambda_0$	6.0
Cylindrical [10]	Aperture	21.1/12.82/27.06/7.54	11.6/7.64/7.01/7.1	$0.44\lambda_0 \times 0.44\lambda_0$	5.0
Ring (Proposed)	Aperture	62.28/25.25	9.49/5.1/5.48	$0.4\lambda_0 \times 0.4\lambda_0$	8.0

6. CONCLUSION

In this article, a ring-shaped ceramic-based antenna with triple-band and dual sense CP features has been designed and examined. Asymmetrical S-shaped aperture coupling creates five different mode patterns inside the ring-shaped ceramic, i.e., ($HEM_{11\delta}$, $HEM_{11\delta+2}$, $HEM_{12\delta\text{-like}}$, $HEM_{12\delta}$, and $HEM_{13\delta}$). A detailed mode analysis is carried out for the proposed antenna design. Additionally, the proposed antenna design offers triple-band dual sense CP waves over the operating bandwidth. Hybrid mode provides the broadsided radiation pattern with good co- to cross-polarization value. These features recommend the proposed antenna design for potential application in WLAN (2.4/5.5 GHz) and WiMAX (3.3/5.0 GHz) wireless networks.

REFERENCES

1. Petosa, A., *Dielectric Resonator Antenna Handbook*, Artech House, Norwood, MA, 2007.
2. Long, S. A., M. W. McAllister, and L. C. Shen, "The resonant cylindrical dielectric cavity antenna," *IEEE Transactions on Antennas and Propagation*, Vol. 31, No. 1, 406–412, 1983.
3. Balanis, C. A., *Antenna Theory: Analysis and Design*, John Wiley and Sons, USA, 2005.
4. Zou, M., J. Pan, L. Zuo, and Z.-P. Nie, "Investigation of a cross-slot-coupled dual-band circularly polarized hybrid dielectric resonator antenna," *Progress In Electromagnetics Research C*, Vol. 53, 187–195, 2014.
5. Pan, Y. M., S. Y. Zheng, and W. Li, "Dual-band and dual-sense omnidirectional circularly polarized antenna," *IEEE Antennas and Wireless Propagation Letters*, Vol. 13, 706–709, 2014.
6. Fang, X., K. W. Leungand, and E. H. Lim, "Singly-fed dual-band circularly polarized dielectric resonator antenna," *IEEE Antennas and Wireless Propagation Letters*, Vol. 13, 995–998, 2014.

7. Altaf, A., J. W. Jung, Y. Yang, K. Y. Lee, and K. C. Hwang, "Reconfigurable dual-/triple-band circularly polarized dielectric resonator antenna," *IEEE Antennas and Wireless Propagation Letters*, Vol. 19, 443–447, 2020.
8. Cheng, C., F. Zhang, Y. Yao, and F. Zhang, "Triband omnidirectional circularly polarized dielectric resonator antenna with top-loaded alford loop," *International Journal of Antennas and Propagation*, 1–8, 2014.
9. Sharma, A., D. K. Tripathi, G. Das, and R. K. Gangwar, "Novel asymmetric Swastik-shaped aperture coupled cylindrical dielectric resonator antenna with dual-band and dual-sense circular polarization characteristics," *Microwave and Optical Technology Letters*, Vol. 61, 405–411, 2018.
10. Sharma, A., G. Das, S. Gupta, and R. K. Gangwar, "Quad-band quad-sense circularly polarized dielectric resonator antenna for GPS/CNSS/WLAN/WiMAX applications," *IEEE Antennas and Wireless Propagation Letters*, Vol. 19, 403–407, 2020.
11. Patel, P., B. Mukherjee, and J. Mukherjee, "Wideband circularly polarized rectangular dielectric resonator antennas using square-shaped slots," *IEEE Antennas and Wireless Propagation Letters*, Vol. 15, 1309–1313, 2015.
12. Sharma, A., G. Das, and R. K. Gangwar, "Composite antenna for ultrawide bandwidth applications: Exploring conceptual design strategies and analysis," *IEEE Antennas and Propagation Magazine*, Vol. 60, 57–65, 2018.
13. Kajfez, D., A. W. Glisson, and J. James, "Computed modal field distributions for isolated dielectric resonators," *IEEE Transaction on Microwave Theory and Techniques*, Vol. 32, 1609–1616, 1984.
14. Guha, D., A. Banerjee, C. Kumar, and Y. M. M. Antar, "Higher order mode excitation for high gain broadside radiation from cylindrical dielectric resonator antennas," *IEEE Transactions on Antennas and Propagation*, Vol. 60, 71–77, 2012.
15. Mongia, R. K. and P. Bhartia, "Dielectric resonator antennas — A review and general design relations for resonant frequency and bandwidth," *International Journal of Microwave and Millimeter-wave Computer-Aided Engineering*, Vol. 4, 230–247, 1994.
16. Guo, L., K. W. Leung, and Y. M. Pan, "Compact unidirectional ring dielectric resonator antennas with lateral radiation," *IEEE Transactions on Antennas and Propagation*, Vol. 63, 5334–5342, 2015.
17. Garg, R., P. Bhartia, I. Bahl, and A. Ittipiboon, *Microstrip Antenna Design Handbook*, Artech House, Norwood, MA, 2001.
18. Faiz, A. M., N. Gogosh, S. A. Khan, and M. F. Shafique, "Effects of an ordinary adhesive material on radiation characteristics of a dielectric resonator antenna," *Microwave and Optical Technology Letters*, Vol. 56, 1502–1506, 2014.
19. Stutzman, W. L. and G. A. Thiele, *Antenna Theory and Design*, A John Wiley & Sons, Hoboken, NJ, 2013.